OPTICA

High-efficiency high-numerical-aperture metalens designed by maximizing the efficiency limit

Shiyu Li, Ho-Chun Lin, and Chia Wei Hsu*

Ming Hsieh Department of Electrical and Computer Engineering, University of Southern California, Los Angeles, California 90089, USA
**cwhsu@usc.edu*

Received 1 December 2023; revised 4 March 2024; accepted 16 March 2024; published 28 March 2024

Theoretical bounds are commonly used to assess the limitations of photonic design. Here we introduce a more active way to use theoretical bounds, integrating them into part of the design process and identifying optimal system parameters that maximize the efficiency limit itself. As an example, we consider wide-field-of-view high-numerical-aperture metalenses, which can be used for high-resolution imaging in microscopy and endoscopy, but no existing design has achieved a high efficiency. By choosing aperture sizes to maximize an efficiency bound, setting the thickness according to a thickness bound, and then performing inverse design, we come up with high-numerical-aperture (NA = 0.9) metalens designs with, to our knowledge, record-high 98% transmission efficiency and 92% Strehl ratio across all incident angles within a 60° field of view, reaching the maximized bound. This maximizing-efficiency-limit approach applies to any multi-channel system and can help a wide range of optical devices reach their highest possible performance.

https://doi.org/10.1364/OPTICA.514907

1. INTRODUCTION

With the rapid advance of nanophotonic design and fabrication, there has been increasing interests in exploring the ultimate limit of device performance. In recent years, theoretical bounds have been proposed for the operational bandwidth [1–5], efficiency (e.g., reflection, transmission, absorption) [6–10], coupling strengths [11,12], energy concentration [13,14], and the device thickness [15,16]. Conventionally, these bounds are used to assess how close a design approaches fundamental limits [17]. One can then set realistic targets and avoid futile attempts on trying to design things that are theoretically impossible. While understanding the limit is important, it would be desirable if theoretical bounds can also play a more active role in improving the design and in pushing the limit itself.

An important application that calls for further progress is designing metalenses with a high numerical aperture (NA) over a wide field of view (FOV) [Fig. 1(a)], which can be used for high-resolution imaging in microscopy, endoscopy, and lithography. Metalenses that offer diffraction-limited resolution at NA $\geq$ 0.9 have been proposed [18–28], with focusing efficiencies exceeding 70% reached through inverse design [29–31]. However, these metalenses are only designed to operate at the normal incidence, and their focusing quality deteriorates sharply at oblique incidence [32,33], severely limiting the angular FOV. There are multiple strategies to broaden the FOV while preserving diffraction-limited focusing, including using an aperture to separate different incident angles onto different parts of the metasurface [34–40], using a doublet [41–47], or stacking multiple structural layers [48]. However, there is ample room for improvement in the efficiency, as summarized in Fig. 1(b) and Supplement 1, Table S1. For NA $\geq$ 0.5, no existing design achieved a focusing efficiency above 50% over a wide FOV.

To identify and to reach the highest possible performance, here we propose to integrate theoretical bounds into part of the design process. In the first step, we consider a recently introduced bound on the channel-averaged transmission efficiency [10], which depends on the sizes of the input and output apertures [D_{in} and D_{out} in Fig. 1(a)]. Given any output aperture D_{out} of interest, we identify the optimal input aperture size $D_{\text{in}}^{\text{opt}}$ that maximizes the efficiency bound. In the second step, we set the thickness h based on a recently introduced bound on the minimal device thickness [15]. In the third step, we perform inverse design using the optimal D_{in} and the minimal h. Applying this approach to a metalens with NA = 0.9 with a 60° FOV, we achieve a transmission efficiency of 98% and Strehl ratio of 92% across the full FOV, reaching the maximized efficiency limit. Previous inverse designs attained significantly lower efficiencies because without the guidance from theoretical bounds, they invariably adopted suboptimal geometry parameters. Both bounds we employ [10,15] follow from the target functionality of any linear multi-channel optical system, so the proposed strategy here is general, not limited to metalens designs.

2. NUMERICAL OPTIMIZATION METHOD

We first describe our inverse design methodology. We employ free-form topology optimization [49–52], allowing non-intuitive permittivity profiles. We have made our code open-source, available at Ref. [53]. We consider the transverse magnetic waves

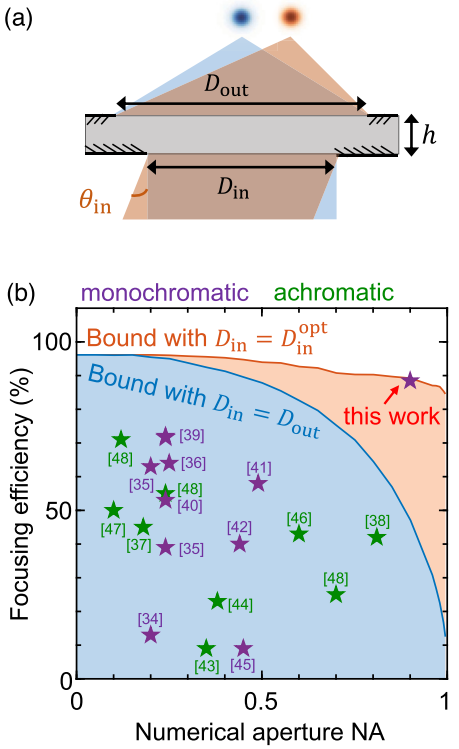

Fig. 1. (a) Schematic of a high-NA wide-field-of-view metalens, with D_{in} (D_{out}), θ_{in}, and h denoting the input (output) aperture diameter, incident angle, and lens thickness. (b) Comparison of the focusing efficiency in existing wide-FOV metalens designs and in this work (purple for monochromatic, green for achromatic). Details are listed in Supplement 1, Table S1. Solid lines show the theoretical limit [10] with $D_{in} = D_{out}$ and with the optimal $D_{in} = D_{in}^{opt}$ used here.

$(E_x, H_y, H_z)(y, z)$ of a system invariant in the x dimension. Given the a-th incident angle θ_{in}^a within the FOV, the desired focal spot position is $\mathbf{r}_f^a = (y = f \tan\theta_{in}^a, z = f)$, where f is the focal length. We quantify the focusing quality by the ratio between the intensity of the actual design at $\mathbf{r}_f^a$ and the focal spot intensity for an ideal lens (i.e., perfectly transmitting and free of aberrations) as

$$I_a = \frac{|E_x(y = f\tan\theta_{in}^a, z = f; \theta_{in}^a)|^2}{\max_y |E_{x,\text{ideal}}(y, z = f; \theta_{in}^a)|^2} = \text{SR}_a \cdot T_a, \quad (1)$$

which is the product of the Strehl ratio (SR) and the transmission efficiency T at incident angle θ_{in}^a. The SR [48,54] is defined as the actual intensity at the focal spot divided by the peak intensity of an ideal diffraction-limited focus normalized by the total transmitted power of the metalens. The transmission efficiency T is the total transmitted power divided by the incident power.

We map out the focal intensity as a function of the incident angle through the generalized transmission matrix $\mathbf{t} = \mathbf{C}\mathbf{A}^{-1}\mathbf{B}$ of the metalens [33]. Here, matrix $\mathbf{A} = -\nabla^2 - (2\pi/\lambda)^2\varepsilon_r(\mathbf{r})$ is the discretized Maxwell differential operator on $E_x(y, z)$ at wavelength λ for the metalens structure defined by its relative permittivity profile $\varepsilon_r(\mathbf{r})$. The a-th column of the M-column input matrix $\mathbf{B} = [\mathbf{B}_1, \cdots, \mathbf{B}_M]$ contains the source profile that generates an incident plane wave at the a-th incident angle θ_{in}^a within the input aperture. This source profile is obtained by projecting $\exp(ik_y^a y)w(y)$ onto the set of propagating plane waves $\{\exp(ik_y^{a'} y)\}$ with $|k_y^{a'}| < 2\pi/\lambda$, where $w(y)$ is a square window function within $|y| < D_{in}/2$. The b-th row of the M-row output projection matrix $\mathbf{C} = [\mathbf{C}_1; \cdots; \mathbf{C}_M]$ performs angular spectrum propagation [55] that propagates E_x on the output surface of the metalens to position $\mathbf{r}_f^b$ on the focal plane. Then, the diagonal elements t_{aa} are the field amplitudes $E_x(\mathbf{r}_f^a; \theta_{in}^a)$ at the focal spots in Eq. (1), for all incident angles $\{\theta_{in}^a\}$ within the FOV of interest. More details are given in Supplement 1, Sections 1 and 2.

To reach the optimal $I_a = \text{SR}_a \cdot T_a$ for all incident angles, we maximize the worst case, $\min_a I_a$, within the FOV. To make the objective function differentiable, we cast the problem into an equivalent epigraph form [56] using a dummy variable g:

$$\max_{g,\varepsilon_r} g, \quad \text{subject to } g \le I_a(\varepsilon_r). \quad (2)$$

We perform the optimization using the gradient-based method of moving asymptotes [57] implemented in the open-source package NLopt [58]. Under finite-difference discretization with grid size Δx, the gradient of I_a with respect to the permittivity profile ε_r of the metalens is calculated via the adjoint method (see Supplement 1, Section 3) as

$$\frac{dI_a}{d\varepsilon_r(\mathbf{r})} = \frac{2k_0^2\Delta x^2 \text{Re}\left[(\mathbf{C}_a\mathbf{A}^{-1}\mathbf{B}_a)^*(\mathbf{A}^{-1}\mathbf{C}_a^{\mathrm{T}} \circ \mathbf{A}^{-1}\mathbf{B}_a)\right](\mathbf{r})}{\max_y |E_{x,\text{ideal}}(y, z = f; \theta_{in}^a)|^2}, \quad (3)$$

where $k_0 = 2\pi/\lambda$ is the free-space wave vector; operators $\circ$, *, and $^{\mathrm{T}}$ stand for the element-wise Hadamard product, complex conjugation, and vector transpose, respectively. We perform the computation with the open-source multi-channel Maxwell solver MESTI [59] using single-precision arithmetic.

During the optimizations, we update the permittivity profile with a macropixel size of $4\Delta x = \lambda/10$ to reduce the dimension of the design space and to keep the minimal feature size large while performing the simulations with a finer resolution of $\Delta x = \lambda/40$ for accuracy. Since the desired response is symmetric, we impose $\varepsilon_r(\mathbf{r})$ to be mirror-symmetric with respect to the lens center $y = 0$ and only parameterize ε_r of the macropixels in the left half of the metalens [red box in Fig. 3(a)] as the optimization variables [60].

3. VALIDATION OF THEORETICAL BOUNDS

Before integrating theoretical bounds into the design process, it is prudent to first verify whether the bounds we use are valid and if they are tight. Such a validation is nontrivial and requires inverse design, since intuition-based designs are not likely to reach these bounds. For this validation, we consider a relatively small system: metalenses with NA = 0.9, FOV = 60°, and output diameter $D_{out} = 16\lambda$. Note that when a lens is used for imaging, the most relevant parameters are the spatial size of the focus, the working distance, and the total number of resolvable points. With diffraction-limited focusing, these parameters together specify the NA, D_{out}, and FOV, while the size D_{in} of the input aperture remains a free variable.

In Ref. [10], we derived that the transmission efficiency averaged over all input channels within the FOV, $\langle T \rangle$, cannot exceed N_{eff}/N_{in}. Here, N_{in} is the number of input channels, and the inverse participation ratio $N_{eff} = (\sum_i \sigma_i^2)^2/\sum_i \sigma_i^4$ quantifies the effective number of high-transmission channels using the singular values $\{\sigma_i\}$ of the transmission matrix. After writing down the ideal transmission matrix of diffraction-limited wide-FOV metalenses in air (Supplement 1, Section 2), we plot N_{eff}/N_{in} as the black solid lines in Fig. 2. The efficiency bound N_{eff}/N_{in} depends on

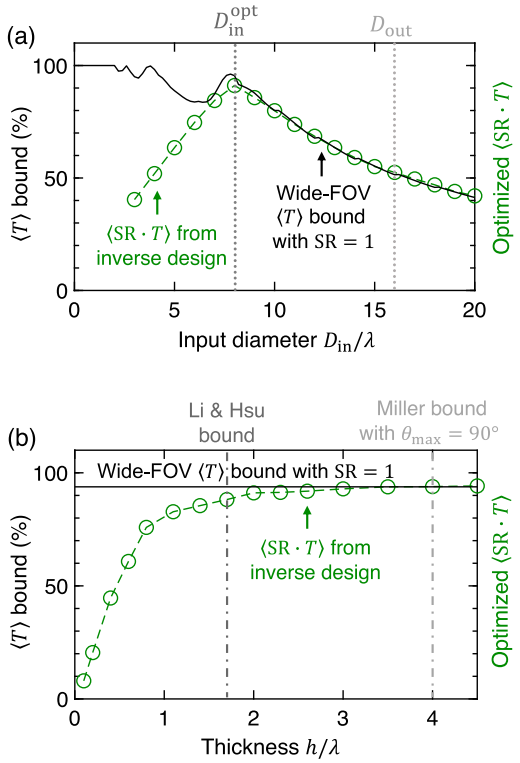

Fig. 2. Validation of theoretical bounds on the channel-averaged total transmission efficiency T and on the device thickness h for a high-NA wide-field-of-view metalens. Black solid lines are bounds on the angle-averaged transmission efficiency $\langle T\rangle$ from Ref. [10], assuming a perfect Strehl ratio SR = 1 across all incident angles within the FOV. Vertical dotted-dashed lines in (b) indicate the thickness bounds from Li and Hsu [15] and from Miller [16]. Green circles are the angle-averaged $\langle \mathrm{SR}\cdot T\rangle$ from gray-scale topology optimizations. Lens parameters: numerical aperture NA = 0.9, output aperture diameter $D_{out} = 16\lambda$, field of view FOV = 60°, refractive index range = [1, 2]. Thickness $h = 2\lambda$ in (a), and input diameter $D_{in} = D_{in}^{opt} = 8\lambda$ in (b).

the diameter D_{in} of the input aperture and has a local maximum at $D_{in} = D_{in}^{opt} \approx 8\lambda$.

To verify this dependence, we perform the topology optimization of Eq. (2) for different D_{in}, with the refractive index of each macropixel bounded within $[n_L, n_H] = [1.0, 2.0]$ and with the metalens thickness being $h = 2\lambda$. The green circles in Fig. 2(a) show the highest $\langle I_a\rangle_a = \langle \mathrm{SR}\cdot T\rangle$ among 100 optimizations with different initial guesses; they agree strikingly well with N_{eff}/N_{in} and exhibit the predicted local maximum at $D_{in} = D_{in}^{opt}$, indicating that this efficiency bound of Ref. [10] is both valid and tight.

Note that N_{eff}/N_{in} is the predicted maximal $\langle T\rangle$ with the Strehl ratio fixed at $\mathrm{SR}_a = 1$ for all incident angles, while the inverse design here allows SR_a to vary and optimizes the worst-case $\mathrm{SR}\cdot T$. Therefore, the optimized $\langle \mathrm{SR}\cdot T\rangle$ should only be compared to N_{eff}/N_{in} when the optimized Strehl ratio is high. For small values of D_{in} here, none of the optimizations reached a high Strehl ratio, presumably because incident light in the overly small aperture D_{in} cannot spread enough to cover the much larger D_{out} to yield the ideal output.

Next, we consider two bounds on the device thickness [15,16]. In Ref. [15], Li and Hsu used the lateral spreading ΔW of spatially localized inputs to quantify the degree of nonlocality, bounding the thickness through an empirical relation $h \geq h_{min}^{Li\&Hsu} = \Delta W$. In Ref. [16], Miller considered a transverse aperture that divides the system and used the number C of channels that cross the transverse aperture to quantify the degree of nonlocality, bounding the thickness with a diffraction heuristics $h \geq h_{min}^{Miller} = (C\lambda)/[2(1-\cos\theta_{max})n_H]$. Here, we take the "maximal internal angle" to be $\theta_{max} = 90°$ since an inhomogeneous refractive index profile can scatter light to all possible angles; using a smaller θ_{max} will increase h_{min}^{Miller}. With the lens parameters here ($D_{out} = 16\lambda$, NA = 0.9, and FOV = 60°), the Li and Hsu bound yields $h_{min}^{Li\&Hsu} = 1.7\lambda$, and the Miller bound yields $h_{min}^{Miller} = 4\lambda$. These bounds are shown as vertical dotted-dashed lines in Fig. 2(b). Note that the value of h_{min}^{Miller} also implicitly depends on how the channel number C is counted, as detailed in Supplement 1, Section 4.

The green circles in Fig. 2(b) show the highest optimized $\langle \mathrm{SR}\cdot T\rangle$ among 100 initial guesses with $D_{in} = D_{in}^{opt} = 8\lambda$. The optimized efficiency is low when the thickness is smaller than $h_{min}^{Li\&Hsu}$. When the thickness goes above $h_{min}^{Li\&Hsu}$, the optimized $\langle \mathrm{SR}\cdot T\rangle$ converges toward N_{eff}/N_{in}, validating both the efficiency bound and the thickness bound. In this example, $h_{min}^{Li\&Hsu}$ marks the transition between low-efficiency and high-efficiency designs, while h_{min}^{Miller} coincides with the thickness at which the efficiency bound N_{eff}/N_{in} is reached.

4. HIGH-NA HIGH-EFFICIENCY METALENS GUIDED BY THEORETICAL BOUNDS

Having verified the theoretical bounds, we now integrate them into the design process. We still consider NA = 0.9 and FOV = 60°, but increase the system size to $D_{out} = 50\lambda$ since parameter scanning is no longer needed. In the first step, we choose $D_{in} = D_{in}^{opt} = 25\lambda$, which maximizes the efficiency bound N_{eff}/N_{in}. In the second step, we choose the necessary thickness. For this system size, we find $h_{min}^{Li\&Hsu} = 5\lambda$ and $h_{min}^{Miller} = 4.5\lambda$ (Supplement 1, Section 4), and we use the larger one $h = h_{min}^{Li\&Hsu} = 5\lambda$ for the inverse design. Finally, in the third step, we perform topology optimization. Here, we additionally include a regularizer in the objective function of the optimization to promote a binary design with $\sqrt{\varepsilon_r(\mathbf{r})}$ being either n_L or n_H (Supplement 1, Section 5). We launch 100 optimizations with random initial guesses and take the best case.

Visualization 1 shows the evolution of the metalens structure, its Strehl ratio, and transmission efficiency as a function of the incident angle, and the intensity profiles at the focal plane as the optimization progresses. Figure 3 shows the final configuration and performance. The Strehl ratio and transmission efficiency both exhibit a flat distribution across the target FOV, with $\langle T\rangle = 98\%$, $\langle \mathrm{SR}\rangle = 92\%$, and $\langle \mathrm{SR}\cdot T\rangle = 90\%$. A tight, near-ideal, focus with a full-width at half maximum (FWHM) of around 0.55λ is achieved for all incident angles within the FOV [Figs. 3(c) and 3(d)]. Visualization 2 plots the 2D field and intensity profiles at all incident angles.

Integration of the theoretical bounds into the design process is crucial in enabling this optimal performance. Previous inverse designs all adopted the common choice of $D_{in} = D_{out}$. Figures 4(a) and 4(b) show the optimized results—following identical optimization steps—when we use $D_{in} = D_{out} = 50\lambda$ with $h = \lambda$ and $h = 5\lambda$. The optimized transmission efficiency $\langle T\rangle$ and Strehl ratio $\langle \mathrm{SR}\rangle$ are both greatly reduced. The thickness choice is also critical. Figure 4(c) shows the optimized results when a typical thickness $h = \lambda$ is used together with $D_{in} = D_{in}^{opt} = 25\lambda$, which is better

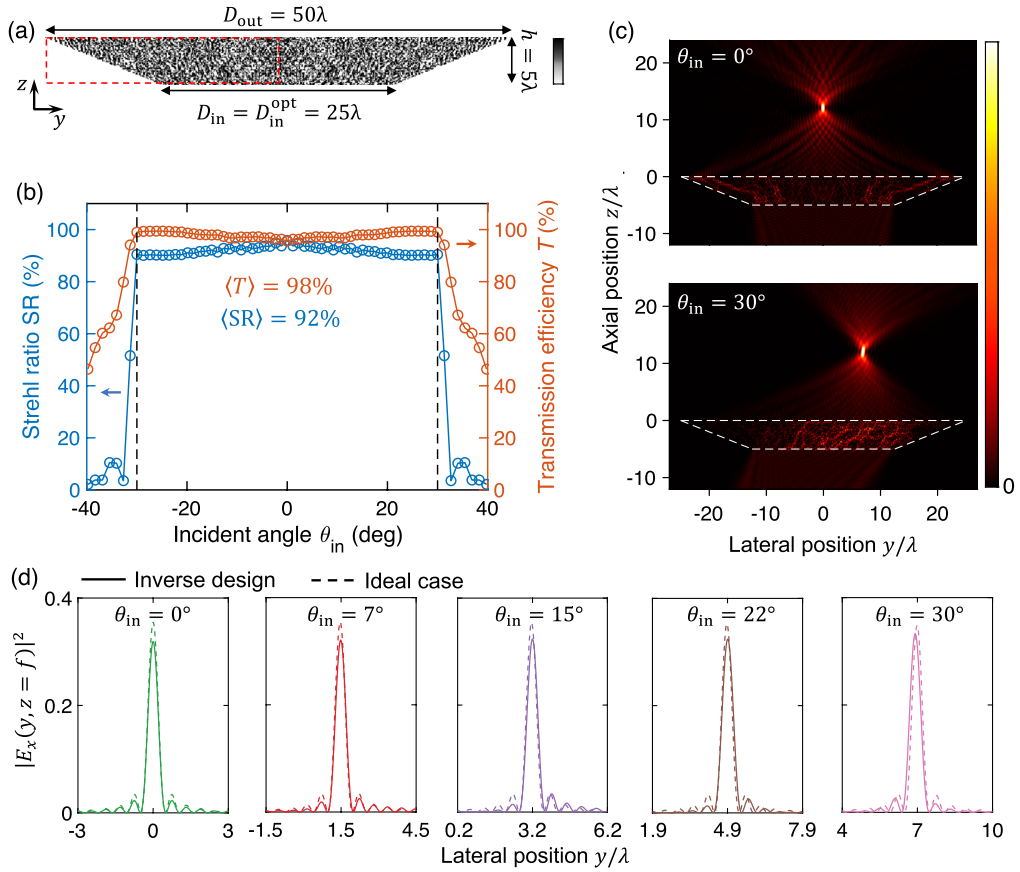

Fig. 3. Inverse-designed high-NA wide-FOV metalens guided by theoretical bounds. (a) Optimized metalens structure, with color indicating the refractive index (between 1.0 and 2.0). (b) Strehl ratio SR and transmission efficiency T of the optimized metalens as a function of the incident angle θ_{in}. Vertical dashed lines mark the FOV. (c) Intensity profiles $|E_x(y, z)|^2$ for incident angles $\theta_{in} = 0°$ and 30°. White dashed lines mark the boundary of the metalens. See Visualization 2 for the field and intensity profiles at all angles. (d) Intensity profiles at the focal plane $z = f$ for different incident angles, comparing outputs from the designed structure (solid lines) with the ideal outputs assuming perfect transmission and perfect Strehl ratio (dashed lines). Lens parameters: NA = 0.9, FOV = 60°, $D_{out} = 50\lambda$, $D_{in} = D_{in}^{opt} = 25\lambda$, $h = h_{min}^{Li\&Hsu} = 5\lambda$.

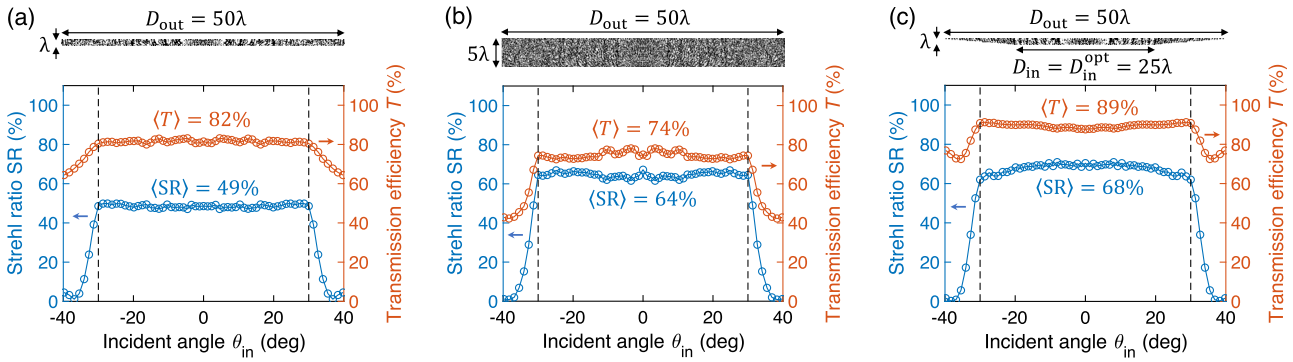

Fig. 4. Inverse-designed metalenses without guidance by theoretical bounds. The lens parameters and optimization procedure are identical to those of Fig. 3 except that $D_{in} = D_{out} = 50\lambda$ in (a), (b) and the thickness is reduced to $h = \lambda$ in (a), (c).

than with $D_{in} = D_{out}$ but still falls substantially below the optimal performance of Fig. 3 where the thickness bound is adopted.

Given the non-convexity of the optimization problem, the optimized result depends on the initial guess, which is chosen randomly here. Supplement 1, Fig. S7 shows a histogram of the final $\langle SR \cdot T \rangle$ among the 100 optimization runs for the four geometries in Figs. 3 and 4.

While the combination of Strehl ratio and transmission efficiency offers a comprehensive set of metrics, their measurement requires high-resolution large-area detectors and is not convenient. Therefore, a more commonly reported metric is the focusing efficiency, defined as the ratio between the transmitted flux within three FWHMs around the focal peak and the incident flux [25,26,31,44,46]. We choose not to optimize such a focusing efficiency here because doing so may encourage the optimization to expand the FWHM and capture more light within the inflated 3× FWHM, which increases the focusing efficiency under such definition but lowers the actual focusing quality. To facilitate comparison

with prior designs, we evaluate the focusing efficiency of the design in Fig. 3 (whose FWHM of 0.55λ is diffraction-limited); the angular dependence is shown in Supplement 1, Fig. S6. The focusing efficiency here averages to 88.5% over the 60° FOV, which is higher even compared to the normal-incidence focusing efficiency of previous narrow-FOV metalenses (see Supplement 1, Table S2).

We also evaluate the ideal focusing efficiency by taking the product of the transmission efficiency bound $N_{\text{eff}}/N_{\text{in}}$ and the focusing efficiency of an ideal focus with unity transmission; such an upper bound on the focusing efficiency is shown as solid lines in Fig. 1(b) for $D_{\text{in}} = D_{\text{out}}$ and $D_{\text{in}} = D_{\text{in}}^{\text{opt}}$. The design in Fig. 3 saturates the maximized upper bound.

5. OUTLOOK

This work shows that theoretical bounds can play an active role in photonic design, identifying optimal system parameters and maximizing the efficiency limit itself. The two bounds we employ [10,15] come from writing down the transmission matrix for the target function, so the strategy here may be applied to a wide range of multi-channel optical systems.

Two-layer systems, such as aperture-stop-based metasurfaces [34–40] and metasurface doublets [41–47], are simpler to design and fabricate. To separate light coming from different angles, such two-layer structures will require a larger distance between layers [39] than the generic thickness bound [15]. Since the efficiency bound [10] applies to any structure including layered ones, one can still use the maximizing-efficiency-bound strategy to determine the optimal aperture size. It will be interesting to explore how close layered structures can approach the general efficiency limit.

The design of full 3D structures is also an important future direction. The procedure for establishing bounds and maximizing the efficiency limit is the same as in 2D: one can still write down the target transmission matrix in 3D, just with more channels to account for the additional dimension and polarization. The computing cost of the inverse design is currently the bottleneck for large-area structures in 3D. One can reduce the computing cost by considering axisymmetric structures [48,61] and by dividing the structure into smaller segments [30,62–64].

Since we only consider one wavelength in this work, the performance of the resulting design is expectedly narrowband (Supplement 1, Fig. S8). Another direction for future work is to tackle broadband designs. To do so, one may consider an additional bandwidth bound [1–4] or adopt a multi-functional bound [65] when looking for the optimal parameters.

Funding. Sony; National Science Foundation (ECCS-2146021).

Acknowledgment. Computing resources are provided by the Center for Advanced Research Computing at the University of Southern California.

Disclosures. The authors declare no conflicts of interest.

Data availability. All data needed to evaluate the conclusions in this study are presented in the paper and Supplement 1. The code is available on GitHub [53].

Supplemental document. See Supplement 1 for supporting content.

REFERENCES

1. S. Shrestha, A. C. Overvig, M. Lu, *et al.*, "Broadband achromatic dielectric metalenses," Light Sci. Appl. **7**, 85 (2018).
2. F. Presutti and F. Monticone, "Focusing on bandwidth: achromatic metalens limits," Optica **7**, 624–631 (2020).
3. J. Engelberg and U. Levy, "Achromatic flat lens performance limits," Optica **8**, 834–845 (2021).
4. K. Shastri and F. Monticone, "Bandwidth bounds for wide-field-of-view dispersion-engineered achromatic metalenses," EPJ Appl. Metamater. **9**, 16 (2022).
5. K. Shastri, O. Reshef, R. W. Boyd, *et al.*, "To what extent can space be compressed? Bandwidth limits of spaceplates," Optica **9**, 738–745 (2022).
6. N. M. Estakhri and A. Alu, "Wave-front transformation with gradient metasurfaces," Phys. Rev. X **6**, 041008 (2016).
7. V. S. Asadchy, M. Albooyeh, S. N. Tcvetkova, *et al.*, "Perfect control of reflection and refraction using spatially dispersive metasurfaces," Phys. Rev. B **94**, 075142 (2016).
8. A. Arbabi and A. Faraon, "Fundamental limits of ultrathin metasurfaces," Sci. Rep. **7**, 43722 (2017).
9. O. Miller, K. Park, and R. A. Vaia, "Towards maximum optical efficiency of ensembles of colloidal nanorods," Opt. Express **30**, 25061–25077 (2022).
10. S. Li and C. W. Hsu, "Transmission efficiency limit for nonlocal metalenses," Laser Photon. Rev. **17**, 2300201 (2023).
11. D. A. Miller, "Waves, modes, communications, and optics: a tutorial," Adv. Opt. Photon. **11**, 679–825 (2019).
12. Z. Kuang and O. D. Miller, "Bounds on the coupling strengths of communication channels and their information capacities," in *Conference on Lasers and Electro-Optics (CLEO)* (IEEE, 2022), paper JTu3A.51.
13. H. Zhang, C. W. Hsu, and O. D. Miller, "Scattering concentration bounds: brightness theorems for waves," Optica **6**, 1321–1327 (2019).
14. H. Shim, H. Chung, and O. D. Miller, "Maximal free-space concentration of electromagnetic waves," Phys. Rev. Appl. **14**, 014007 (2020).
15. S. Li and C. W. Hsu, "Thickness bound for nonlocal wide-field-of-view metalenses," Light Sci. Appl. **11**, 338 (2022).
16. D. A. Miller, "Why optics needs thickness," Science **379**, 41–45 (2023).
17. P. Chao, B. Strekha, R. K. Defo, *et al.*, "Physical limits in electromagnetism," Nat. Rev. Phys. **4**, 543–559 (2022).
18. A. Arbabi, Y. Horie, A. J. Ball, *et al.*, "Subwavelength-thick lenses with high numerical apertures and large efficiency based on high-contrast transmitarrays," Nat. Commun. **6**, 7069 (2015).
19. W. T. Chen, A. Y. Zhu, M. Khorasaninejad, *et al.*, "Immersion metalenses at visible wavelengths for nanoscale imaging," Nano Lett. **17**, 3188–3194 (2017).
20. H. Liang, Q. Lin, X. Xie, *et al.*, "Ultrahigh numerical aperture metalens at visible wavelengths," Nano Lett. **18**, 4460–4466 (2018).
21. R. Paniagua-Dominguez, Y. F. Yu, E. Khaidarov, *et al.*, "A metalens with a near-unity numerical aperture," Nano Lett. **18**, 2124–2132 (2018).
22. N. Mohammad, M. Meem, B. Shen, *et al.*, "Broadband imaging with one planar diffractive lens," Sci. Rep. **8**, 2799 (2018).
23. H. Chung and O. D. Miller, "High-NA achromatic metalenses by inverse design," Opt. Express **28**, 6945–6965 (2020).
24. Y.-Q. Liu, J. Sun, Y. Che, *et al.*, "High numerical aperture microwave metalens," Opt. Lett. **45**, 6262–6265 (2020).
25. D. Sang, M. Xu, M. Pu, *et al.*, "Toward high-efficiency ultrahigh numerical aperture freeform metalens: from vector diffraction theory to topology optimization," Laser Photon. Rev. **16**, 2200265 (2022).
26. Y. Wang, M. Peng, W. Cheng, *et al.*, "Manipulation force analysis of nanoparticles with ultra-high numerical aperture metalens," Opt. Express **30**, 28479–28491 (2022).
27. M. Yang, X. Shen, Z. Li, *et al.*, "High focusing efficiency metalens with large numerical aperture at terahertz frequency," Opt. Lett. **48**, 4677–4680 (2023).
28. W. Xue, H. Zhang, A. Gopal, *et al.*, "Fullwave design of CM-scale cylindrical metasurfaces via fast direct solvers," arXiv, arXiv:2308.08569 (2023).
29. S. J. Byrnes, A. Lenef, F. Aieta, *et al.*, "Designing large, high-efficiency, high-numerical-aperture, transmissive meta-lenses for visible light," Opt. Express **24**, 5110–5124 (2016).
30. T. Phan, D. Sell, E. W. Wang, *et al.*, "High-efficiency, large-area, topology-optimized metasurfaces," Light Sci. Appl. **8**, 48 (2019).
31. S. Banerji, M. Meem, A. Majumder, *et al.*, "Imaging with flat optics: metalenses or diffractive lenses?" Optica **6**, 805–810 (2019).
32. A. Kalvach and Z. Szabó, "Aberration-free flat lens design for a wide range of incident angles," J. Opt. Soc. Am. B **33**, A66–A71 (2016).
33. H.-C. Lin, Z. Wang, and C. W. Hsu, "Fast multi-source nanophotonic simulations using augmented partial factorization," Nat. Comput. Sci. **2**, 815–822 (2022).

34. J. Engelberg, C. Zhou, N. Mazurski, *et al.*, "Near-IR wide-field-of-view Huygens metalens for outdoor imaging applications," Nanophotonics **9**, 361–370 (2020).
35. M. Y. Shalaginov, S. An, F. Yang, *et al.*, "Single-element diffraction-limited fisheye metalens," Nano Lett. **20**, 7429–7437 (2020).
36. C.-Y. Fan, C.-P. Lin, and G.-D. J. Su, "Ultrawide-angle and high-efficiency metalens in hexagonal arrangement," Sci. Rep. **10**, 15677 (2020).
37. F. Yang, S. An, M. Y. Shalaginov, *et al.*, "Design of broadband and wide-field-of-view metalenses," Opt. Lett. **46**, 5735–5738 (2021).
38. J. Qi, Y. Wang, C. Pang, *et al.*, "Broadband wide field-of-view metalens by the virtual-diffraction-aperture method," ACS Photon. **9**, 3668–3678 (2022).
39. F. Yang, S. An, M. Y. Shalaginov, *et al.*, "Understanding wide field-of-view flat lenses: an analytical solution," Chin. Opt. Lett. **21**, 023601 (2023).
40. H.-I. Lin, J. Geldmeier, E. Baleine, *et al.*, "Wide field-of-view, large-area long-wave infrared silicon metalenses," arXiv, arXiv:2307.12974 (2023).
41. A. Arbabi, E. Arbabi, S. M. Kamali, *et al.*, "Miniature optical planar camera based on a wide-angle metasurface doublet corrected for monochromatic aberrations," Nat. Commun. **7**, 13682 (2016).
42. B. Groever, W. T. Chen, and F. Capasso, "Meta-lens doublet in the visible region," Nano Lett. **17**, 4902–4907 (2017).
43. D. Tang, L. Chen, J. Liu, *et al.*, "Achromatic metasurface doublet with a wide incident angle for light focusing," Opt. Express **28**, 12209–12218 (2020).
44. C. Kim, S.-J. Kim, and B. Lee, "Doublet metalens design for high numerical aperture and simultaneous correction of chromatic and monochromatic aberrations," Opt. Express **28**, 18059–18076 (2020).
45. Z. Li, C. Wang, Y. Wang, *et al.*, "Super-oscillatory metasurface doublet for sub-diffraction focusing with a large incident angle," Opt. Express **29**, 9991–9999 (2021).
46. Z. Huang, M. Qin, X. Guo, *et al.*, "Achromatic and wide-field metalens in the visible region," Opt. Express **29**, 13542–13551 (2021).
47. J. Jang, G.-Y. Lee, Y. Kim, *et al.*, "Dispersion-engineered metasurface doublet design for broadband and wide-angle operation in the visible range," IEEE Photon. J. **15**, 2201209 (2023).
48. Z. Lin, C. Roques-Carmes, R. E. Christiansen, *et al.*, "Computational inverse design for ultra-compact single-piece metalenses free of chromatic and angular aberration," Appl. Phys. Lett. **118**, 041104 (2021).
49. M. P. Bendsoe and O. Sigmund, *Topology Optimization: Theory, Methods, and Applications* (Springer, 2003).
50. O. D. Miller, *Photonic Design: From Fundamental Solar Cell Physics to Computational Inverse Design* (University of California, 2012).
51. S. Molesky, Z. Lin, A. Y. Piggott, *et al.*, "Inverse design in nanophotonics," Nat. Photonics **12**, 659–670 (2018).
52. J. A. Fan, "Freeform metasurface design based on topology optimization," MRS Bull. **45**, 196–201 (2020).
53. S. Li, "Inverse design of wide-FOV metalens," GitHub (2024), https://github.com/complexphoton/metalens_inverse_design.
54. J. Bentley and C. Olson, *Field Guide to Lens Design* (SPIE, 2012).
55. J. W. Goodman, *Introduction to Fourier Optics*, 4th ed. (W. H. Freeman, 2017).
56. S. P. Boyd and L. Vandenberghe, *Convex Optimization* (Cambridge University, 2004).
57. K. Svanberg, "A class of globally convergent optimization methods based on conservative convex separable approximations," SIAM J. Optim. **12**, 555–573 (2002).
58. "The NLopt nonlinear-optimization package," https://github.com/stevengj/nlopt.
59. "MESTI," https://github.com/complexphoton/MESTI.jl.
60. S. Li, H.-C. Lin, and C. W. Hsu, "Fast multi-channel inverse design through augmented partial factorization," ACS Photon. **11**, 378–384 (2024).
61. C. Roques-Carmes, Z. Lin, R. E. Christiansen, *et al.*, "Toward 3D-printed inverse-designed metaoptics," ACS Photon. **9**, 43–51 (2022).
62. Z. Lin and S. G. Johnson, "Overlapping domains for topology optimization of large-area metasurfaces," Opt. express **27**, 32445–32453 (2019).
63. M. Torfeh and A. Arbabi, "Modeling metasurfaces using discrete-space impulse response technique," ACS Photon. **7**, 941–950 (2020).
64. J. Skarda, R. Trivedi, L. Su, *et al.*, "Low-overhead distribution strategy for simulation and optimization of large-area metasurfaces," NPJ Comput. Mater. **8**, 78 (2022).
65. H. Shim, Z. Kuang, Z. Lin, *et al.*, "Fundamental limits to multi-functional and tunable nanophotonic response," Nanophotonics (2024).